RSC Advances

PAPER

View Article Online
View Journal | View Issue

Cite this: *RSC Adv.*, 2020, **10**, 35265

$Co_{1-x}Ba_xFe_2O_4$ ($x = 0$, 0.25, 0.5, 0.75 and 1) nanoferrites as gas sensor towards NO_2 and NH_3 gases

Hariom Pawar,[a] Meenu Khan,[a] Chhavi Mitharwal,[b] U. K. Dwivedi,[a] Supratim Mitra[b] and Deepshikha Rathore *[a]

Received 14th May 2020
Accepted 2nd August 2020

DOI: 10.1039/d0ra04303f

rsc.li/rsc-advances

$Co_{1-x}Ba_xFe_2O_4$ ($x = 0$, 0.25, 0.5, 0.75 and 1) nanoferrites were synthesized using a controlled chemical co-precipitation technique. Their structural, optical, dielectric and gas sensing properties were characterized by X-ray diffractometry, UV-Vis spectroscopy and an LCR meter with a gas sensing unit. The crystalline sizes were estimated using the Scherrer formula and were found to be 7.8 nm, 14.4 nm, 21.8 nm, 16.5 nm and 30.3 nm for $x = 0$, 0.25, 0.5, 0.75 and 1, respectively. The fundamental optical band gaps were calculated by extrapolating the linear part of $(\alpha h\upsilon)^2$ *vs.* $h\upsilon$ of the synthesized nanoferrites. The SEM and EDX spectra also confirmed the formation of nanoferrites. Dramatic behavior was observed in the dielectric constant and dissipation factor with varying temperature, which provides a substantial amount of information about electric polarization. The synthesized nanoferrites were tested towards NO_2 and NH_3 gases. The order of sensitivity (%) towards NH_3 was analyzed as $x = 0.75 > x = 0.5 > x = 0.25 > x = 0 > x = 1$, while the order was $x = 0 > 0.75 > 1 > 0.5 > 0.25$ for NO_2 gas.

1. Introduction

Modern research to cultivate gas sensors and biosensor fabrication technology using nanoferrite materials is looking forward to artificial building blocks with combinations of two or more different types of nanoferrites.[1,2] The choice of specific nanoferrites in a definite molar ratio may enhance the physical and chemical properties of new developed architectures at the atomic scale. The synthesis of nanoferrites is readily accomplished by "bottom up" approaches such as sol–gel, chemical co-precipitation, hydrothermal, and micro-emulsion techniques.[3] The size of the nanoferrites plays a vital role in sensing technology. Their sensing properties can be enhanced by varying several physical parameters, such as temperature, time, and pressure, and chemical parameters, such as molar ratio, concentration, and the nature of the reaction.[4] Nanoferrites are very promising materials for gas sensing properties because of their normal and inverse spinel structures and high physical and chemical stability in open atmosphere.

Prasad *et al.*[5] synthesized $CoFe_2O_4$ fiber using the electrospinning method and characterized its structural, morphological and magnetic properties. They applied the $CoFe_2O_4$ fiber as a sensing material for ammonia gas at room temperature with a very small concentration of ammonia (at 25 ppm) rather than other test gases, such as acetone, ethanol, 2-propanol and methanol. Zhang *et al.*[6] studied the formation of $CoFe_2O_4$ nanoparticles using modified solvothermal and microwave-assisted solvothermal methods and found higher sensitivity towards acetone vapor at 200 °C with low concentrations up to 5 ppm. Bodade *et al.*[7] reported the preparation of $CoFe_2O_4$ doped with different wt% of Ni and Sm using a sol–gel citrate method and its structural, morphological and electrical properties. They found that the 10 wt% Ni and 0.2 wt% Sm doped $CoFe_2O_4$ showed higher sensitivity and selectivity towards H_2S gas than other reducing gases. Khan *et al.*[8] studied the synthesis of $CoFe_2O_4$/SiC nanocomposites by a chemical co-precipitation method with various wt% of SiC. They found that the dielectric properties, a.c. conductivity and sensitivity (%) for NH_3 gas were higher for 20 wt% of CFO/SiC nanocomposites than for nanocomposites with other wt%. Khandekar *et al.*[9] reported the preparation of nanocrystalline $CoFe_{2-x}Ce_xO_4$ ferrites ($x = 0$, 0.04, 0.08) by a molten salt method; they observed that at $x = 0.04$, the $CoFe_{2-x}Ce_xO_4$ ferrites showed excellent sensitivity and selectivity towards acetone gas at 250 °C.

Karmakar *et al.*[10] reported the formation of barium hexaferrites by a solid state method and their properties. They also reported the sensing properties of barium hexaferrites towards volatile organic compounds such as acetone and ethanol by varying the reaction temperature and gas concentration, and they found fast response for both vapors at a very low concentration (20 ppm). Peng *et al.*[11] reported the synthesis of $Bi_{1-x}La_xFeO_3$ ($x = 0$–0.2) using a sol–gel method; they found it to be a prominent material for the fabrication of chemiresistive sensors, which showed the highest sensitivity and selectivity

[a]*Amity School of Applied Sciences, Amity University Rajasthan, Jaipur 303002, Rajasthan, India. E-mail: deep.nano@gmail.com*
[b]*Department of Physics, Banasthali University, Niwai, 304022, Rajasthan, India*

towards acetone gas. Sen *et al.*[12] studied the development of $BaCa_2Fe_{16}O_{27}$ hexaferrite by a simple sol–gel technique and observed that the $BaCa_2Fe_{16}O_{27}$ hexaferrite sensor showed high sensitivity, good reproducibility, rapid response/recovery times and stability towards ethanol at 100 ppm compared to other volatile organic compounds such as acetone, methane and carbon monoxide gases.

Many ferrite nanoparticles[13–18] have been tested towards reducing and toxic gases as gas sensors as well as towards contamination in food as biosensors;[19] however, enhancement of the sensitivity, selectivity and lifetime of existing sensors is still an important issue. Ba-substituted cobalt ferrite at Co sites has not been reported in the literature to date. For this purpose, $Co_{1-x}Ba_xFe_2O_4$ (x = 0, 0.25, 0.5, 0.75 and 1) nanoferrites have been synthesized by a chemical co-precipitation method at room temperature and tested towards NO_2 and NH_3 gases, including their structural, optical and dielectric properties as well as their a.c. conductivity. To the best of our knowledge, the developed $Co_{1-x}Ba_xFe_2O_4$ nanoferrite at x = 0.75 is a novel combination of normal and inverse spinel ferrites with unique properties and has the highest sensitivity towards NO_2 and NH_3 gases at room temperature. The $Co_{1-x}Ba_xFe_2O_4$ (x = 0, 0.25, 0.5, 0.75 and 1) nanoferrites may also show response towards coronavirus-2019 (COVID-19), which has become an epidemic disease.

2. Experimental details

$Co_{1-x}Ba_xFe_2O_4$ (x = 0, 0.25, 0.5, 0.75 and 1) nanoferrites were synthesized by chemical co-precipitation. $CoCl_2\cdot 6H_2O$ (CDH), $BaCl_2\cdot 2H_2O$ (Fisher Scientific) and $FeCl_3\cdot 6H_2O$ (Rankem) were used as precursors while maintaining a molar ratio of 1 : 2 of Co/Ba : Fe. The combinations of aqueous solutions of $CoCl_2\cdot 6H_2O$ with 1, 0.25, 0.5, 0.75 and 0 M and $BaCl_2\cdot 2H_2O$ with 0, 0.75, 0.5, 0.25 and 1 M concentrations, respectively, were prepared in separate beakers, and prepared 2 M $FeCl_3\cdot 6H_2O$ was added to form 5 separate complex mixtures. Further, the prepared complex mixtures were added dropwise to an alkaline solution of 0.8 M NaOH (CDH) under strong stirring with a uniform speed. The experiment was performed at room temperature. Stirring was continued for 30 minutes after the last drop of aqueous solution of the mixture was added to the alkaline medium. The precipitate was initially brown in color; after completion of the reaction, it became reddish brown. The precipitate was collected by centrifugation and washed four times to remove impurities, then dried for 1 hour at 200 °C. After drying, the $Co_{1-x}Ba_xFe_2O_4$ (x = 0, 0.25, 0.5, 0.75 and 1) nanoferrites were ground with a mortar and pestle and sintered for 1 hour at 200 °C.

The structural and phase formation analysis of $Co_{1-x}Ba_xFe_2O_4$ (x = 0, 0.25, 0.5, 0.75 and 1) nanoferrites were studied using a Bruker diffractometer, Model D8 Advance, with Cu K_α radiation in the range of 20° to 80° at a scan rate of 0.05° s^{-1} and a 40 kV operating voltage with 40 mA current. The optical properties were studied using a UV-visible spectrophotometer, Thermo Scientific Model BIOMAT 3S, in the range of 200 nm to 600 nm. Morphological and elemental analyses were performed by scanning electron microscopy (TESCAN MIRA) and energy dispersive X-ray studies (OXFORD XMAX). The dielectric properties were studied using a HIOKI LCR meter (IM3536) at different temperatures from 30 °C to 100 °C and a frequency range from 40 Hz to 8 MHz, and the gas sensing properties were investigated using a gas sensing setup with a temperature controller and LCR meter. A KBR hydraulic press was used to obtain pellets of the prepared nanocomposites with diameters of 10 mm and thicknesses of 2 mm. The disk-shaped pellets were coated on both sides with silver paste to endow the sides with conductivity and were connected with copper wire. Hence, parallel plate capacitor devices were designed.

3. Results and discussion

3.1 Structural properties

The XRD patterns of the $Co_{1-x}Ba_xFe_2O_4$ (x = 0, 0.25, 0.5, 0.75 and 1) nanoferrites are exhibited in Fig. 1. It can be observed from Fig. 1(a and e) that synthesized nanoparticles at x = 0 and 1 can be identified as $CoFe_2O_4$ (JCPDS no. 00-022-1086) and $BaFe_2O_4$ (JCPDS no. 46-0113), which show pure single-phase cubic and orthorhombic structures, respectively. It is depicted in Fig. 1(b–d) that as the concentration increases from x = 0.25 to 0.75, the peaks of $CoFe_2O_4$ and $BaFe_2O_4$ appear in their correct positions at 2θ = 23.999°, 27.469°, 34.444°, 35.452°, 41.893°, 44.650°, 46.934° and 63.004°, which confirms the formation of $Co_{1-x}Ba_xFe_2O_4$ (x = 0.25, 0.5 and 0.75) nanoferrites. The average particle size was calculated using the Scherrer formula:[20]

$$D = \frac{0.89\lambda}{\beta \cos\theta} \quad (1)$$

where D is the particle size, λ is the X-ray wavelength, θ is Bragg's angle and β is the FWHM. The calculated particle sizes of the $Co_{1-x}Ba_xFe_2O_4$ (x = 0, 0.25, 0.5, 0.75 and 1.0) nanoferrites were 7.8 nm, 14.4 nm, 21.8 nm, 16.5 nm and 30.3 nm, respectively.

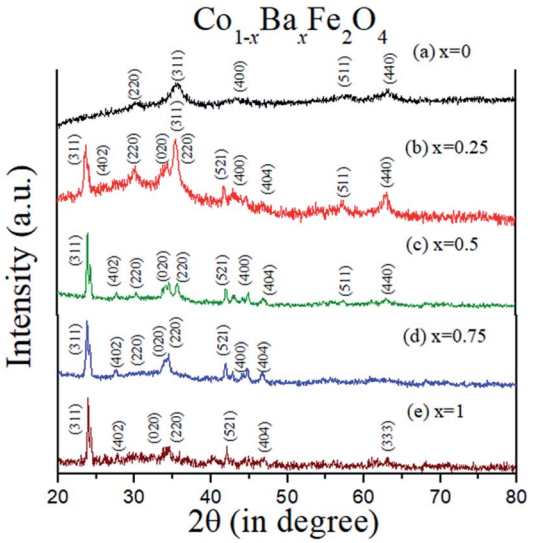

Fig. 1 XRD patterns of the $Co_{1-x}Ba_xFe_2O_4$ (x = 0, 0.25, 0.5, 0.75 and 1) nanoferrites.

3.2 Optical properties

The optical absorbance spectra of the $Co_{1-x}Ba_xFe_2O_4$ (x = 0, 0.25, 0.5, 0.75 and 1) nanoferrites are illustrated in Fig. 2. It can be observed from Fig. 2 that the fundamental absorption edges of the $Co_{1-x}Ba_xFe_2O_4$ (x = 0, 0.25, 0.5, 0.75 and 1) nanoferrites were found to be approximately 215 ± 2 nm, 215 ± 2 nm, 217 ± 2 nm, 216 ± 2 nm and 236 ± 2 nm, respectively. For the photon energies E, the absorbance can be calculated by the given formula:[21]

$$\alpha = \frac{A(h\upsilon - E_g)^{1/2}}{h\upsilon} \quad (2)$$

where α is the absorbance, A is a constant, E_g is the energy band gap, h is the Planck constant and υ is the frequency of light.

The obtained optical band gaps (E_g) from an extrapolation of the linear region of the plot of $(\alpha h\upsilon)^2$ *vs.* $h\upsilon$ at different concentrations of Ba^{2+} ion (x = 0, 0.25, 0.5, 0.75 and 1) in the $Co_{1-x}Ba_xFe_2O_4$ nanoferrites are illustrated in Fig. 3. The optical band gap (E_g) values of the $Co_{1-x}Ba_xFe_2O_4$ (x = 0, 0.25, 0.5, 0.75 and 1) nanoferrites were found to be 3.48 eV, 3.15 eV, 3.45 eV, 3.65 eV and 4.01 eV, respectively. The changes in the optical band gap are due to the substitution of Ba^{2+} ions at the positions of the Co^{2+} ions with increasing concentration of Ba^{2+} ions from x = 0 to x = 1. $CoFe_2O_4$ and $BaFe_2O_4$ nanoferrites possess indirect energy band gaps. The intense hybridized Co + O and Ba + O valance edges allow both $O_p \rightarrow Co_d$ and $Co_d \rightarrow Co_d$ transitions in $CoFe_2O_4$ nanoferrites and $O_p \rightarrow Ba_s$ and $Ba_s \rightarrow Ba_s$ transitions in $BaFe_2O_4$ nanoferrites. Consequently, the localized Co and Ba states near the valence band edge can create inter-site d → d and s → s excitations, analogous to the transitions of the p → d and p → s sub orbitals. Transitions in the marginal channels (Co + O → Fe (O_h)) and (Ba + O → Fe (O_h)) separately and transitions between both channels define the fundamental indirect band gap and absorption edge.[22] From Fig. 3, it can be observed that the fundamental band gaps of pure $CoFe_2O_4$ and $BaFe_2O_4$ are 3.48 eV and 4.01 eV, respectively. As the doping of Ba^{2+} ions into $CoFe_2O_4$ nanoferrites increased at x = 0.25, 0.5 and 0.75, the calculated band gaps were found to be 3.15 eV, 3.45 eV and 3.65 eV, respectively. The enrichment in the band gap with increasing concentration of Ba^{2+} ions may be due to the quantum confinement effect in the nano range.

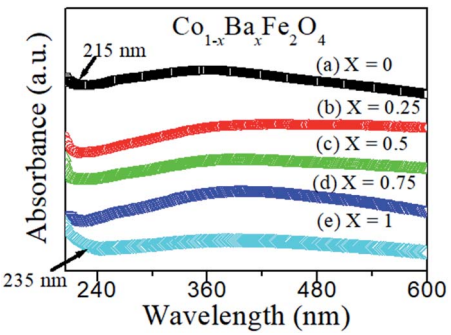

Fig. 2 Optical absorbance spectra of the $Co_{1-x}Ba_xFe_2O_4$ (x = 0, 0.25, 0.5, 0.75 and 1) nanoferrites.

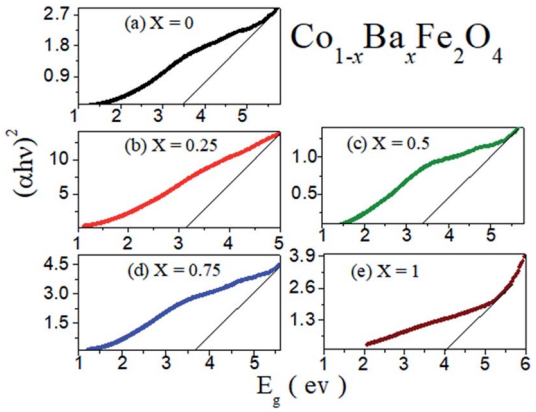

Fig. 3 Optical band gaps of the $Co_{1-x}Ba_xFe_2O_4$ (x = 0, 0.25, 0.5, 0.75 and 1) nanoferrites.

3.3 Morphological and elemental analysis

The morphologies of the $Co_{1-x}Ba_xFe_2O_4$ (x = 0, 0.25, 0.5, 0.75 and 1) nanoferrites were investigated using SEM, and the micrographs are shown in Fig. 4(a–e). Clusters of nanoparticles were observed in all the micrographs. The effects of the $BaFe_2O_4$ nanoparticles can be clearly seen in Fig. 4(b–d). The EDX spectra of the $Co_{1-x}Ba_xFe_2O_4$ (x = 0, 0.25, 0.5, 0.75 and 1) nanoferrites are depicted in Fig. 5(a–e). The energy dispersive X-ray data revealed the formation of $Co_{1-x}Ba_xFe_2O_4$ (x = 0, 0.25, 0.5, 0.75 and 1) nanoferrites with high purity. It can be observed from Fig. 4 and 5 that as the concentration increases, the substitution of Co^{2+} by Ba^{2+} increases.

3.4 Dielectric properties

The dielectric properties were investigated over the fabricated capacitor devices using the formula:[23]

$$\varepsilon_r = \frac{Ct}{\varepsilon_0 A} \quad (3)$$

where ε_r is the dielectric constant of the sample, ε_0 is the permittivity of free space, C is the capacitance of the capacitor, t is the thickness of the pellet and A is the area of the pellet.

The dielectric constants as a function of frequency with varying temperatures from 30 °C to 100 °C of $Co_{1-x}Ba_xFe_2O_4$ (x = 0, 0.25, 0.5, 0.75 and 1) are illustrated in Fig. 6(a–e). It can be observed from Fig. 6 that the dielectric constant decreases gradually as the frequency increases up to 0.5 MHz and then becomes almost constant upon increasing the frequency from 0.5 MHz to 8 MHz for all compositions; this is because at high frequency, the dipoles stop their orientation in the direction of the applied field, due to which the polarization vanishes.[24] It can also be observed from Fig. 6(a–e) that as the temperature increases from 30 °C to 40 °C, the value of the dielectric constant increases in all compositions except x = 1 and decreases with increasing temperature from 40 °C to 100 °C. For x = 1, the values of the dielectric constant are very similar at 30 °C and 50 °C, while the value of dielectric is lower at other temperatures. This may be because of the normal spinel structure of $BaFe_2O_4$. The charge carrier mobility increases with

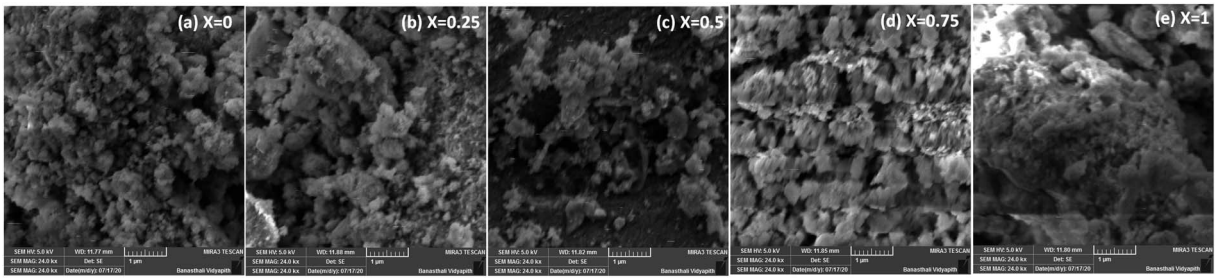

Fig. 4 SEM images of the $Co_{1-x}Ba_xFe_2O_4$ (x = 0, 0.25, 0.5, 0.75 and 1) nanoferrites.

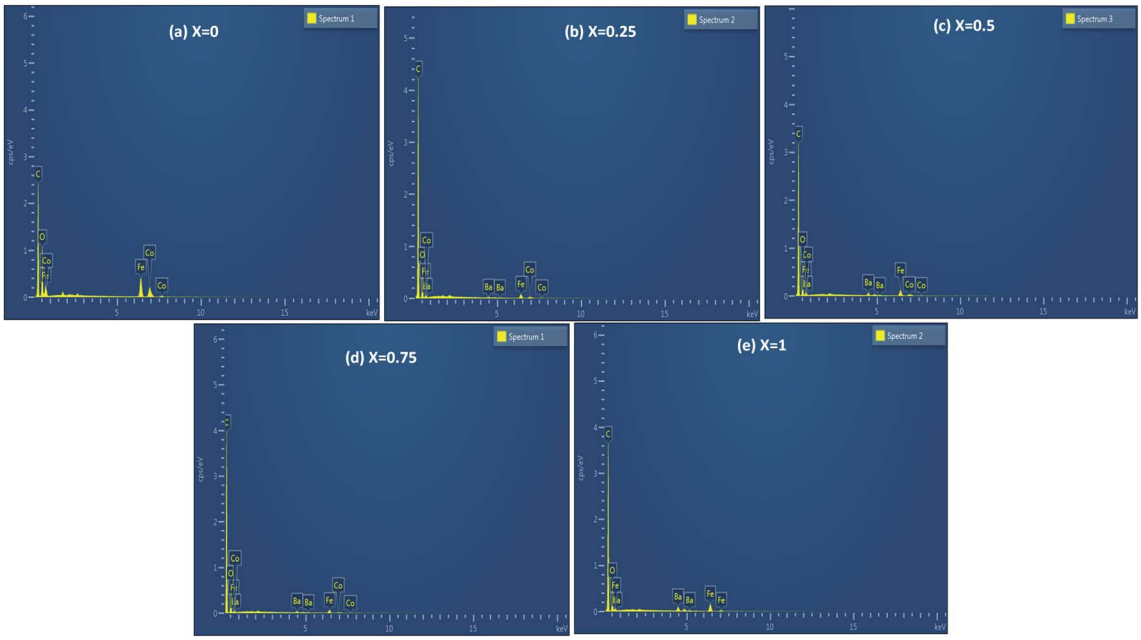

Fig. 5 EDX spectra of the $Co_{1-x}Ba_xFe_2O_4$ (x = 0, 0.25, 0.5, 0.75 and 1) nanoferrites.

increasing temperature up to 40 °C and 50 °C in the cases of inverse and normal spinel structures, respectively. Upon further increase in temperature, the anisotropy increases because of rearrangement of the dipoles in the direction of the electric field, due to which the dielectric polarization starts to decrease; this results in a low dielectric constant.

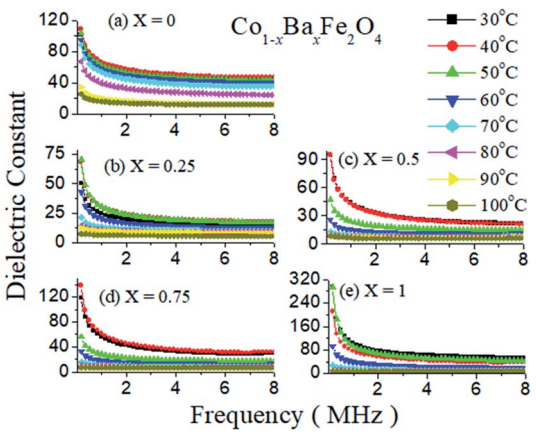

Fig. 6 Dielectric constants as a function of frequency of the $Co_{1-x}Ba_xFe_2O_4$ (x = 0, 0.25, 0.5, 0.75 and 1) nanoferrites.

Furthermore, Fig. 6(a and e) show the dielectric studies of pure $CoFe_2O_4$ and $BaFe_2O_4$, which have maximum dielectric constant values of 108 and 210, respectively, at a temperature of 30 °C. The dielectric constant decreases at $x = 0.25$ and starts to increase with increasing concentration up to $x = 1$. This dramatic change in the dielectric constant may occur due to the mixed inverse and normal spinel structures of the prepared nanoferrites. The reason for the increase in the dielectric constant may be the exchange of electrons and holes in n-type and p-type ferrite, *i.e.* doping of Ba^{2+} in $CoFe_2O_4$ at large concentrations enhances the exchange of electrons in Fe^{3+} and converts it to Fe^{2+} with hole transfer from Co^{3+} to Co^{2+}. These electron–hole exchange phenomena increase the polarization in the nanoferrites, which increases the value of the dielectric constant.[24]

The dissipation factor is also an important characteristic feature of dielectric materials. The dissipation factors as a function of frequency of the $Co_{1-x}Ba_xFe_2O_4$ (x = 0, 0.25, 0.5,

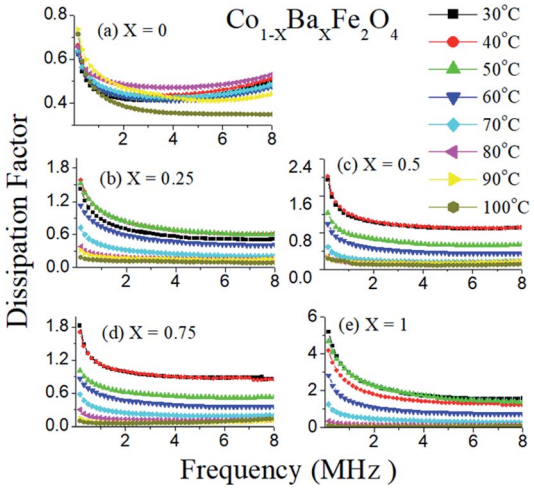

Fig. 7 Dissipation factors with frequency of the $Co_{1-x}Ba_xFe_2O_4$ ($x = 0$, 0.25, 0.5, 0.75 and 1) nanoferrites at different temperature from 30 °C to 100 °C.

0.75 and 1) nanoferrites at different temperatures from 30 °C to 100 °C are shown in Fig. 7(a–e). It can be observed from Fig. 7(a–e) that the dissipation factor decreases as the frequency increases up to 1 MHz and then becomes constant from 1 MHz to 8 MHz in all compositions. Consequently, very interesting behavior of the dissipation factor can be found with varying temperature in Fig. 7. The dissipation factor is larger at higher temperatures (except 100 °C) in the entire frequency range for $x = 0$ and it decreases sequentially (except at 50 °C) on increasing temperature for $x = 1$. The dissipation factor is similar but higher at 40 °C to 50 °C for $x = 0.25$ compared to a temperature of 30 °C, while it is almost the same at 30 °C and 40 °C for $x = 0.5$ and $x = 0.75$. As the concentration of Ba^{2+} ion increases towards the Co^{2+} sites in $CoFe_2O_4$, the dissipation factor simultaneously decreases with increasing temperature and becomes almost constant at 100 °C. Therefore, all dielectric experiments were performed up to 100 °C.

3.4.1 A.C. conductivity measurements. The a.c. conductivities of the $Co_{1-x}Ba_xFe_2O_4$ ($x = 0$, 0.25, 0.5, 0.75 and 1) nanoferrites in the temperature range from 30 °C to 100 °C with the log of the frequency were calculated using the given formula:[25]

$$\sigma_{a.c.}(\omega) = \omega\varepsilon_0\varepsilon_r \tan\delta \quad (4)$$

where $\sigma_{a.c.}(\omega)$ is the a.c. conductivity in the presence of the angular frequency, ω is the angular frequency, ε_0 is the permittivity of free space, ε_r is the dielectric constant of the material and tan δ is the dissipation factor of the material.

The a.c. conductivities as a function of log of frequency with temperature variation from 30 °C to 100 °C of the $Co_{1-x}Ba_x$-Fe_2O_4 ($x = 0$, 0.25, 0.5, 0.75 and 1.0) nanoferrites are revealed in Fig. 8. It can be observed from Fig. 8 that the a.c. conductivity reaches a maximum at 30 °C and 40 °C for $x = 0$, 0.5 and 0.75, while it is higher at 30 °C and 50 °C for $x = 0.25$ and 1. On increasing the temperature up to 100 °C, the a.c. conductivity decreases in all the samples. It is also illustrated in Fig. 8 that at a lower frequency, the a.c. conductivity is smaller and almost constant; it increases with increasing frequency and possesses the highest value at 8 MHz in all compositions. This increment in the a.c. conductivity occurs, because on increasing frequency, the hopping mechanism increases at the atomic level.

In a dielectric material, the total a.c. conductivity does not depend on the d.c. conductivity because there are few free charge carriers present. Hence, the amount of d.c. conductivity was found to be negligible. The total a.c. conductivity can be calculated by the given equation:[25]

$$\sigma_{a.c.} = Af^p \quad (5)$$

where A is the coefficient that defines the strength of polarizability, f is a frequency applied by an instrument and p is another coefficient which is calculated from the slope given by the straight-line equation:[25]

$$\log \sigma_{a.c.} = \log A + p \log f \quad (6)$$

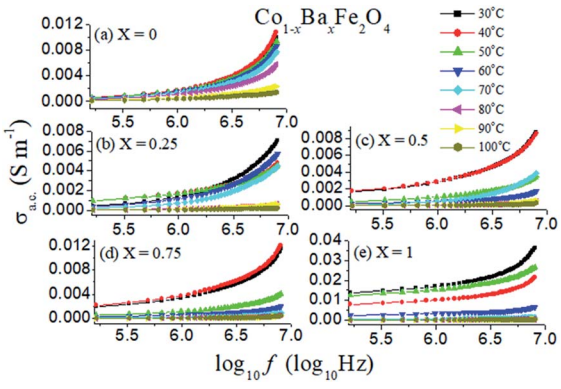

Fig. 8 A.C. conductivities of the $Co_{1-x}Ba_xFe_2O_4$ ($x = 0$, 0.25, 0.5, 0.75 and 1) nanoferrites with varying temperature from 30 °C to 100 °C with log of frequency.

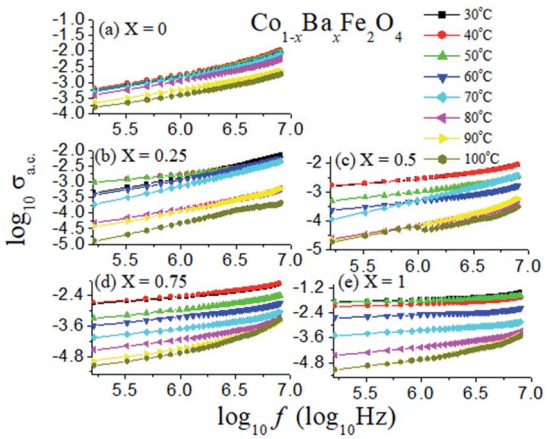

Fig. 9 Log of a.c. conductivity as a function of log of frequency in the temperature range from 30 °C to 100 °C of the $Co_{1-x}Ba_xFe_2O_4$ ($x = 0$, 0.25, 0.5, 0.75 and 1) nanoferrites.

Table 1 Frequency exponent factor (slope p) and pre-exponent factor A for $Co_{1-x}Ba_xFe_2O_4$ (x = 0, 0.25, 0.5, 0.75 and 1) nanoferrites at a different temperature range

S. no.	$Co_{1-x}Ba_xFe_2O_4$	Temperature (in °C)	p	A
1	$x = 0$	30	0.76758	4.07×10^{-8}
2		40	0.76758	4.07×10^{-8}
3		50	0.73017	6.98×10^{-8}
4		60	0.73318	6.14×10^{-8}
5		70	0.71656	7.26×10^{-8}
6		80	0.70326	6.92×10^{-8}
7		90	0.60521	1.38×10^{-8}
8		100	0.65695	4.32×10^{-8}
1	$x = 0.25$	30	0.73719	5.27×10^{-8}
2		40	0.41409	5.68×10^{-6}
3		50	0.4076	6.18×10^{-6}
4		60	0.72509	5.23×10^{-8}
5		70	0.83325	7.54×10^{-9}
6		80	0.65284	1.63×10^{-8}
7		90	0.72203	5.41×10^{-9}
8		100	0.71339	2.55×10^{-9}
1	$x = 0.5$	30	0.4548	5.40×10^{-6}
2		40	0.44201	6.60×10^{-6}
3		50	0.50137	1.03×10^{-6}
4		60	0.52397	3.49×10^{-7}
5		70	0.9176	1.66×10^{-9}
6		80	0.82434	8.06×10^{-10}
7		90	0.86706	4.50×10^{-10}
8		100	0.68731	3.90×10^{-10}
1	$x = 0.75$	30	0.03585	4.84×10^{-6}
2		40	0.46617	6.20×10^{-6}
3		50	0.53997	6.49×10^{-7}
4		60	0.52384	4.12×10^{-7}
5		70	0.60095	4.96×10^{-8}
6		80	0.75514	2.23×10^{-9}
7		90	0.96594	5.39×10^{-11}
8		100	1.17559	2.19×10^{-12}
1	$x = 1$	30	0.26896	4.20×10^{-4}
2		40	0.2703	2.40×10^{-4}
3		50	0.20723	8.80×10^{-4}
4		60	0.27069	7.60×10^{-5}
5		70	0.37035	3.43×10^{-6}
6		80	0.68084	7.61×10^{-9}
7		90	1.02869	1.70×10^{-11}
8		100	1.02078	1.80×10^{-11}

The log of the a.c. conductivity of the $Co_{1-x}Ba_xFe_2O_4$ ($x = 0$, 0.25, 0.5, 0.75 and 1) nanoferrites in the temperature range from 30 °C to 100 °C with the log of the frequency was investigated and is shown in Fig. 9. It can be analyzed from Fig. 9 that the plots of all the compositions at different temperatures are nearly parallel to each other. The values of the slope p are tabulated in Table 1. The value of the pre-exponent factor A varies from 10^{-4} to 10^{-11} with varying temperature of the $Co_{1-x}Ba_xFe_2O_4$ ($x = 0$, 0.25, 0.5, 0.75 and 1) nanoferrites.

3.5 Gas sensing properties

3.5.1 Gas preparation. Oxidizing gas (NO_2) was prepared by reacting Cu metal with concentrated NH_4OH at 45 °C and was collected in a round bottom flask. Similarly, reducing gas (NH_3) was obtained by heating liquid ammonia at 30 °C to 40 °C. The reaction mechanisms are given by relations (7) and (8):

$$NH_{3(aq.)} \xrightarrow{\text{heating}} NH_{3(g)} \quad (7)$$

$$Cu_{(s)} + 2HNO_{3(aq.)} \xrightarrow{45\ ^\circ C} (CuNO)_{2(aq.)} + H_2O_{(l)} + NO_2 \quad (8)$$

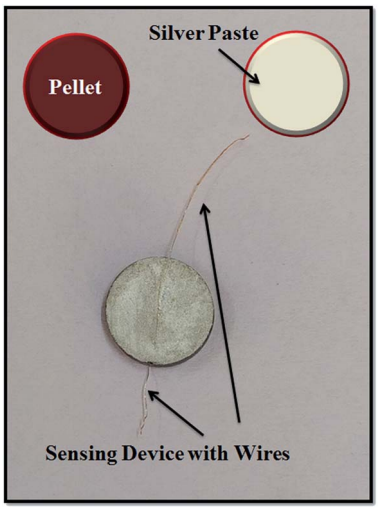

Fig. 10 Image of the gas sensing device.

3.5.2 Gas sensing phenomenon. The phenomenon of gas sensitivity on the prepared nanoferrite devices can be demonstrated with the aid of the adsorption and desorption processes. The oxygen adsorbs on the sensing device in air atmosphere and desorbs in the presence of gases; this provides an electron, which can travel on the surface of the sensing material and causes a change in the resistance. The sensitivities of the test gases on the surface of the sensing device were calculated by the following relations:[26]

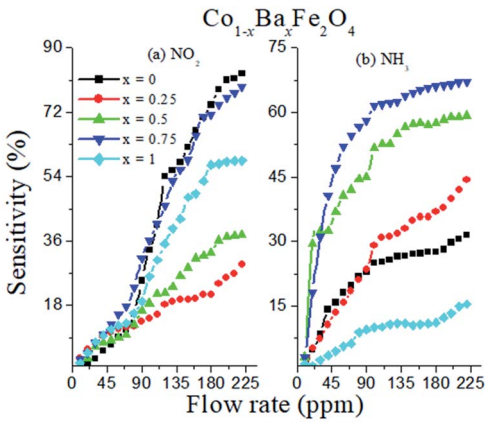

Fig. 11 Sensitivity (%) as a function of flow rate (ppm) of the $Co_{1-x}Ba_xFe_2O_4$ (x = 0, 0.25, 0.5, 0.75 and 1) nanoferrites towards NO_2 and NH_3 gases.

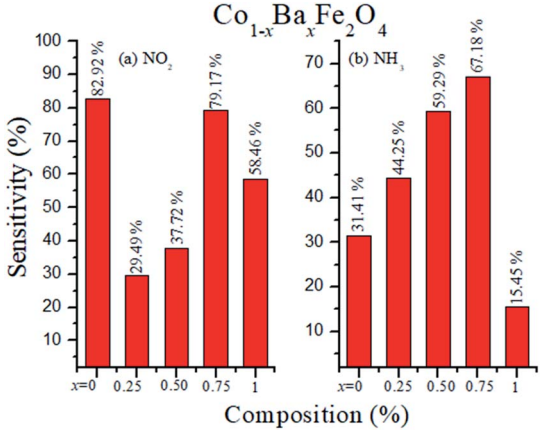

Fig. 12 Selectivity (%) of the $Co_{1-x}Ba_xFe_2O_4$ ($x = 0$, 0.25, 0.5, 0.75 and 1) nanoferrites towards (a) NO_2 and (b) NH_3 gases.

$$S(\%) = \left(\frac{\Delta R}{R_g}\right) \times 100 = \left(\frac{R_a \sim R_g}{R_g}\right) \times 100 \quad \text{if} \quad R_g > R_a \tag{9}$$

$$S(\%) = \left(\frac{\Delta R}{R_a}\right) \times 100 = \left(\frac{R_a \sim R_g}{R_a}\right) \times 100 \quad \text{if} \quad R_a > R_g \tag{10}$$

where S (%) is the sensitivity of the test gas, ΔR is the change in resistance, R_a is the resistance of air and R_g is the resistance of the test gas.

The fabricated capacitor device with the $Co_{1-x}Ba_xFe_2O_4$ ($x = 0$, 0.25, 0.5, 0.75 and 1) nanoferrites, shown in Fig. 10, was tested towards NO_2 and NH_3 gases. The sensitivity (%) as a function of the flow rate in ppm (parts per million) is illustrated in Fig. 11. It can be observed from Fig. 11 that the composition $x = 1$ responded quickly at a low flow rate of NO_2 gas, while the sensitivity (%) followed the sequence of $x = 0 > x = 0.75 > x = 1 > x = 0.5 > x = 0.25$ at a 220 ppm flow rate of NO_2 gas. The responses of $x = 0$ and $x = 1$ towards NH_3 gas were found to be 31.41% and 15.45%, as shown in Fig. 12, and the order was $x = 0.75 > x = 0.5 > x = 0.25 > x = 0 > x = 1$ towards NH_3 gas at a 220 ppm flow rate. The composition with $x = 0.75$ exhibited the highest sensitivity (67.18%) for NH_3 gas and (79.17%) for NO_2 gas at a 220 ppm flow rate. The value of the resistance decreased in all compositions towards NH_3 gas from flow rates of 10 ppm to 220 ppm; therefore, it can be said that the all synthesized nanoferrites behave like n-type semiconductors in an NH_3 gas environment. The same behavior was demonstrated by all nanoferrites except for the composition with $x = 1$ towards NO_2 gas. NO_2 is a strong oxidizing agent with higher electrophilic properties; therefore, it adsorbs faster on the surface of $BaFe_2O_4$, even in the absence of oxygen. The reaction mechanism is given in eqn (11) and (12).[27,28] The oxidation of NO_2 leads to the reduction of conduction electrons in the conduction band, which increases the resistance of $Co_{1-x}Ba_xFe_2O_4$ at $x = 1$.[29] Eqn (13) describes how NO_2 is directly adsorbed on the Ba^{2+} sites by electron capture and desorbed as NO.

$$NO_{2(gas)} + e_{(surface)}^{-} \rightarrow NO_{2(adsorbed)}^{-} \tag{11}$$

$$NO_{2(gas)} + O_{2(adsorbed)}^{-} + 2e_{(surface)}^{-} \rightarrow NO_{2(adsorbed)}^{-} + 2O_{(adsorbed)}^{-} \tag{12}$$

$$\left\{ NO_{2(gas)} + Ba^{2+} \xrightarrow{\text{adsorption}} \left(Ba^{3+} - NO_2^{-}\right) \xrightarrow{\text{adsorption}} \left(Ba^{3+} - O^{-}\right) \right.$$
$$\left. + NO \quad 2\left(Ba^{3+} - O^{-}\right) \xrightarrow{\text{adsorption}} Ba^{2+} + O_2 \right\} \tag{13}$$

It can be observed from Fig. 11 that at a higher flow rate (220 ppm), the sensitivity (%) becomes constant; this is because of the complete adsorption and desorption process between the surface oxygen and inlet (NO_2 and NH_3) gases. Therefore, the experiment was performed up to a 220 ppm flow rate.

The sensitivity (%) of the $Co_{1-x}Ba_xFe_2O_4$ ($x = 0$, 0.25, 0.5, 0.75 and 1) nanoferrites towards NO_2 and NH_3 gases is depicted in Fig. 12, which indicates that $Co_{1-x}Ba_xFe_2O_4$ showed the best response at $x = 0.75$ for both gases; the order was found to be NO_2 > NH_3 at room temperature. The sensitivity (%) and selectivity responses suggest that $Co_{1-x}Ba_xFe_2O_4$, at $x = 0.75$ is a promising material as a sensor towards NO_2 gas.

3.6 COVID-19 detection

The synthesized $Co_{1-x}Ba_xFe_2O_4$ ($x = 0$, 0.25, 0.5, 0.75 and 1) nanoferrites possess combined properties of inverse and normal spinel structures. Hence, those nanoferrites may act as proficient sensors for COVID-19, which has emerged as a worldwide epidemic disease. For this purpose, the DNA receptors of coronavirus could be implanted on the surface of the above designed gas sensing device; those are produced artificially and matched with the RNA sequences of the coronavirus. The fabricated device could detect the presence of COVID-19 because of the complementary sequences of the virus receptor.[30] The response of the fabricated device towards COVID-19 can be measured in terms of sensitivity (%). Further testing is needed with permission of the government.

4. Conclusions

In this research article, $Co_{1-x}Ba_xFe_2O_4$ ($x = 0$, 0.25, 0.5, 0.75 and 1) nanoferrites were synthesized successfully. The calculated particle sizes were estimated to be 7.8 nm, 14.4 nm, 21.8 nm, 16.5 nm and 30.3 nm for the $Co_{1-x}Ba_xFe_2O_4$ ($x = 0$, 0.25, 0.5, 0.75 and 1) nanoferrites, respectively. Optical absorbance of all the synthesized nanoferrites was obtained in the ultra-violet region. Hence, these nanoferrites can be used as UV absorbers. The energy band gaps were also calculated using the UV-Vis spectra and were found to be 3.48 eV, 3.15 eV, 3.45 eV, 3.65 eV and 4.01 eV, respectively. The SEM and EDX spectra also confirmed the formation of the nanoferrites. The temperature-varying dielectric constants and dissipation factors as a function of frequency provide abundant information about the electric polarization due to the mixture of inverse and normal

spinel structures, which affects the gas sensing properties towards reducing gas (NH_3) and oxidizing gas (NO_2) at room temperature. The a.c. conductivity by varying the log frequency with the frequency exponent factor p and pre-exponent factor A was also illustrated. The sensitivity (%) as a function of flow rate (ppm) was tested towards NO_2 and NH_3 gases. The orders of sensitivity (%) were determined to be $x = 0 > x = 0.75 > x = 1 > x = 0.25 > x = 0.5$ for NO_2 gas and $x = 0.75 > x = 0.5 > x = 0.25 > x = 0 > x = 1$ for NH_3 gas at a 220 ppm flow rate. $Co_{1-x}Ba_xFe_2O_4$ at $x = 0.75$ showed the best response for both gases, and the order was found to be $NO_2 > NH_3$ at room temperature. The optical properties, dielectric properties, sensitivity (%) and selectivity responses suggest that $Co_{1-x}Ba_xFe_2O_4$ at $x = 0.75$ is the most promising material for sensors towards NO_2 gas. Due to their effective response towards gases, nanoferrites may detect COVID-19 as well, for which further study is needed.

Conflicts of interest

There is no any conflict of interest.

Acknowledgements

The authors are thankful to the Science and Engineering Research Board (Project no. EMR/2016/002156) and University Grant Commission, Department of Atomic Energy, Consortium for Scientific Research, Indore (Project no.-CSR-IC/MSRSR-10/CRS-218/2017-18/1299) for providing funds.

References

1 S. L. Hu, J. Liu, H. Y. Yu and Z. W. Liu, *J. Magn. Magn. Mater.*, 2019, **473**, 79–84, DOI: 10.1016/j.jmmm.2018.10.044.
2 H. Pawar, D. Kumar, D. Rathore and U. K. Dwivedi, *Appl. Innov. Res.*, 2019, **1**, 75–77.
3 M. Khan, H. Pawar, M. Kumari, D. Rathore and U. K. Dwivedi, *Appl. Innov. Res.*, 2019, **1**, 93–95, http://nopr.niscair.res.in/handle/123456789/49574.
4 D. Rathore, R. Kurchania and R. K. Pandey, *Invertis Journal of Science and Technology*, 2012, **5**, 132–137, DOI: 10.1109/JSEN.2015.2432035.
5 P. D. Prasad and J. Hemalatha, *J. Magn. Magn. Mater.*, 2019, **484**, 225–233, DOI: 10.1016/j.jmmm.2019.04.026.
6 H. J. Zhang, L. Z. Liu, X. R. Zhang and F. N. Meng, *J. Alloys Compd.*, 2019, **788**, 1103–1112, DOI: 10.1016/j.jallcom.2019.03.009.
7 A. B. Bodade, A. B. Bodade, H. G. Wankhade, G. N. Chaudhari and D. C. Kothari, *Talanta*, 2012, **89**, 183–188, DOI: 10.1016/j.talanta.2011.12.013.
8 M. Khan, H. Pawar, M. Kumari, C. Patra, G. Patel, U. K. Dwivedi and D. Rathore, *J. Alloys Compd.*, 2020, **840**, 155596, DOI: 10.1016/j.jallcom.2020.155596.
9 M. S. Khandekar, N. L. Mulla, I. Suryavasnshi and S. S. Suryavanshi, *Ceram. Int.*, 2014, **40**, 447–452, DOI: 10.1016/j.ceramint.2013.06.021.
10 M. Karmakar, B. Mondal, M. Pal and K. Mukharjee, *Sens. Actuators, B*, 2014, **190**, 627–633, DOI: 10.1016/j.snb.2013.09.035.
11 S. Peng, M. Ma, W. Yang, Z. Wang, J. Bi and J. Wu, *Sens. Actuators, B*, 2020, **313**, 128060, DOI: 10.1016/j.snb.2020.128060.
12 S. Sen, P. Anand, M. Narjinary, S. K. Md Mursalin and R. Manna, *Ceram. Int.*, 2016, **42**, 12581–12585, DOI: 10.1016/j.ceramint.2016.03.201.
13 D. Rathore, R. Kurchania and R. K. Pandey, *J. Mater. Sci.: Mater. Electron.*, 2018, **29**, 1925–1932, DOI: 10.1007/s10854-017-8102-0.
14 D. Rathore and S. Mitra, *J. Appl. Phys.*, 2016, **1728**, 20166, DOI: 10.1063/1.1713501.
15 D. Rathore, R. Kurchania and R. K. Pandey, *IEEE Sens. J.*, 2015, **15**, 4961–4966, DOI: 10.1109/JSEN.2015.2432035.
16 D. Rathore, R. Kurchania and R. K. Pandey, *Sens. Actuators, A*, 2013, **199**, 236–240, DOI: 10.1016/j.sna.2013.06.002.
17 A. A. Bagade, V. V. Ganbavle, S. V. Mohite, T. D. Dongale, B. B. Sinha and K. Y. Rajpure, *J. Colloid Interface Sci.*, 2017, **497**, 181–192, DOI: 10.1016/j.jcis.2017.02.067.
18 M. Dewan and S. B. Majumder, *Materialia*, 2019, **7**, 100363, DOI: 10.1016/j.mtla.2019.100363.
19 P. Singh and D. Rathore, *J. Appl. Phys.*, 2016, **1728**, 20259, DOI: 10.1063/1.4946310.
20 R. Kurchania, D. Rathore and R. K. Pandey, *J. Mater. Sci.: Mater. Electron.*, 2015, **26**, 9355–9365, DOI: 10.1007/s10854-015-3083-3.
21 M. Abdelaziz and M. M. Ghannam, *Phys. B*, 2010, **405**, 958–964, DOI: 10.1016/j.physb.2009.10.030.
22 B. S. Holinsworth, D. Mazumdar, H. Sims, Q. C. Sun, M. K. Yurtisigi, S. K. Sarker, A. Gupta, W. H. Butler and J. L. Musfeldt, *Appl. Phys. Lett.*, 2013, **103**, 082406, DOI: 10.1063/1.4818315.
23 B. D. Cullity, *Element of X-Ray Diffraction, Addison-Wesley Series in Metallurgy and Materials*, London, New York, 2nd edn, 1978.
24 D. Rathore, R. Kurchaniya and R. K. Pandey, *Int. J. Miner., Metall. Mater.*, 2014, **21**, 408–414, DOI: 10.1007/s12613-014-0923-8.
25 D. Rathore, R. Kurchania and R. K. Pandey, *J. Nanosci. Nanotechnol.*, 2013, **13**, 1812–1819, DOI: 10.1166/jnn.2013.7120.
26 D. Rathore, S. Mitra, R. Kurchania and R. K. Pandey, *J. Mater. Sci.: Mater. Electron.*, 2018, **29**, 1925–1932, DOI: 10.1007/s10854-017-8102-0.
27 P. Shankar and J. B. B. Rayappan, *Sci. Lett. J.*, 2015, **4**, 126.
28 C. Lopez Baroni and J. M. Tulliani, *Materials*, 2013, **6**, 4801–4816, DOI: 10.3390/ma6104801.
29 T. Akamatsu, T. Itoh, N. Izu and W. Shin, *Sens. Mater.*, 2013, **13**, 12467–12481, DOI: 10.3390/s130912467.
30 G. Qiu, Z. Gai, Y. Tao, J. Schmitt, G. A. Kullak-Ublick and J. Wang, Dual-Functional Plasmonic Photothermal Biosensors for Highly Accurate Severe Acute Respiratory Syndrome Coronavirus 2 Detection, *ACS Nano*, 2020, **14**(5), 5268–5277, DOI: 10.1021/acsnano.0c02439.

